Imaging lipid bodies in cells and tissues using third-harmonic generation microscopy

Delphine Débarre[1], Willy Supatto[2], Ana-Maria Pena[1], Aurélie Fabre[3], Thierry Tordjmann[4], Laurent Combettes[4], Marie-Claire Schanne-Klein[1] & Emmanuel Beaurepaire[1]

Lipid bodies have an important role in energy storage and lipid regulation. Here we show that lipid bodies are a major source of contrast in third-harmonic generation (THG) microscopy of cells and tissues. In hepatocytes, micrometer-sized lipid bodies produce a THG signal 1–2 orders of magnitude larger than other structures, which allows one to image them with high specificity. THG microscopy with ~1,200 nm excitation can be used to follow the distribution of lipid bodies in a variety of unstained samples including insect embryos, plant seeds and intact mammalian tissue (liver, lung). We found that epi-THG imaging is possible in weakly absorbing tissues because bulk scattering redirects a substantial fraction of the forward-generated harmonic light toward the objective. Finally, we show that the combination of THG microscopy with two-photon and second-harmonic imaging provides a new tool for exploring the interactions between lipid bodies, extracellular matrix and fluorescent compounds (vitamin A, NADH and others) in tissues.

Lipid bodies are ubiquitous structures composed of a neutral lipid core surrounded by phospholipids and associated proteins, and are present in many cells and tissues. Many recent studies indicate that these structures are complex and dynamic organelles that interact with numerous cell components[1,2]. Besides their role in the digestive track[3], lipid bodies participate in the physiology of cells and tissues with many different functions, and are found in several forms such as retinosomes[4], milk fat globules[5] or plant oleosomes[1]. Disorders of lipid regulation occur in widespread diseases, including atherosclerosis, diabetes and steatosis. As lipid bodies are generally not fluorescent, their study usually involves specimen preparation and staining[6], which limits long-term observation of their dynamics and turnover.

An emerging application of multiphoton microscopy[7] is the observation of unstained samples based on endogenous sources of nonlinear signals[8] such as two photon–excited fluorescence (2PEF) and second-harmonic generation (SHG). Combined 2PEF-SHG imaging allows direct visualization of extracellular matrix fibrillar components and of fluorescent cellular species such as NADH, flavins or retinol[8]. Multiphoton microscopy provides enhanced imaging depth in scattering samples, which makes it suitable for studying intact tissues. THG microscopy, a recent evolution of multiphoton microscopy, has been used for mapping optical heterogeneities inside biological samples[9–11]. The nature of the structures that can be detected with this technique, however, has not been addressed precisely.

In this study, we show that micrometer-sized lipid bodies are a major source of contrast in THG images and can be detected with high specificity in a variety of cells and tissues. We use THG microscopy to quantify lipid metabolism in isolated hepatocytes, to track individual lipid bodies in *Drosophila melanogaster* embryos, and to image the distribution of lipid bodies in intact plant and animal tissues. We show that epi-THG imaging is possible in weakly absorbing samples, and we demonstrate specific imaging of extracellular matrix components and endogenous fluorophores along with lipid bodies in fresh lung tissue using multimodal multiphoton microscopy.

RESULTS

Third-order optical properties of biological liquids

In coherent nonlinear microscopies such as SHG, coherent anti-Stokes Raman scattering or THG microscopy, the signal is a coherent superposition of the fields radiated by different objects within the excitation volume. Therefore it critically depends on both the micrometer-scale organization of the scatterers and on the structure of the excitation field. One property of THG microscopy is that no signal is obtained when the beam is focused inside a homogeneous, normally dispersive medium[9,12]. In contrast, the signal is enhanced for interfaces and optical inhomogeneities of size comparable to the beam focus[13,14]. Besides these structural factors, THG is sensitive to local differences in third-order nonlinear susceptibility, refractive index and dispersion. Under moderate focusing conditions (numerical aperture (NA) < 0.8), the signal approximately scales as $(\alpha_o - \alpha_s)^2$, where $\alpha \equiv \chi^{(3)}/n_{3\omega}\,(n_{3\omega} - n_\omega)$, where $\chi^{(3)}$ is the third-order nonlinear susceptibility, $n_{3\omega}$ is the refractive index at the harmonic frequency, $(n_{3\omega} - n_\omega)$ is the refractive index dispersion between the harmonic and the fundamental frequency, and the subscripts o and s refer to the object and

[1]Laboratory for optics and biosciences, Ecole Polytechnique, CNRS, INSERM, F-91128 Palaiseau, France. [2]Laboratory of physico-chemistry of life, CNRS, Institut Curie, F-75005, Paris, France. [3]Pathophysiology and epidemiology of respiratory failure, INSERM, Bichat Hospital, F-75018, Paris, France. [4]Laboratory of cell signaling and calcium, INSERM, Paris XI University, F-91405, Orsay, France. Correspondence should be addressed to E.B. (emmanuel.beaurepaire@polytechnique.edu).

RECEIVED 16 SEPTEMBER; ACCEPTED 6 OCTOBER; PUBLISHED ONLINE 20 DECEMBER 2005; DOI:10.1038/NMETH813

Table 1 | Optical properties of liquids and substrates ($\lambda = 1{,}180$ nm)

	$\alpha = \chi^{(3)} / (n_{3\omega}(n_{3\omega} - n_{\omega}))$ ($\times 10^{-22} m^2/V^2$)	$\chi^{(3)}$ ($\times 10^{-22} m^2/V^2$)	$(n_{3\omega} - n_{\omega})$	$n_{633\ nm}$	$(\alpha - \alpha_{water})^2$
Water	61.8 ± 3.6	1.68 ± 0.08	0.0203[a]	1.332[a]	0
Water and 1 M NaCl	63.9 ± 4.2	1.79 ± 0.09	0.021 ± 0.001	1.344[a]	4.41
Triglycerides	83.7 ± 5.0	2.58 ± 0.5	0.021 ± 0.003	1.465[b] ± 0.005	479.61
Oil	90.0 ± 5.0	2.71 ± 0.5	0.021 ± 0.003	1.435[c] ± 0.005	795.24
Silica	56.21	1.87[d]	0.0226[e]	1.457[e]	31.25
Glass (BK7)	68.22	2.78[d]	0.0266[e]	1.515[e]	41.22

[a]n values from refs. 35,36. [b]European standard for triacetin. [c]French standard. [d]χ value from ref. 34. [e]Schott glass catalog.

its surroundings. Therefore, knowledge of both the linear and nonlinear susceptibility of biological solutions is critical when interpreting THG images. As most of these data were not available in the literature, we first measured the optical properties of water, triglycerides, olive oil, and ionic solutions using the Maker fringe technique[15] (**Table 1**). These data indicate that micrometer-sized lipid bodies included in an aqueous environment should provide a strong source of contrast in THG microscopy because the linear and nonlinear optical properties of lipid solutions greatly differ from those of water. As a comparison, a 1 M ionic solution is much closer to water in terms of dispersion and nonlinear susceptibility. Therefore, the signal obtained from intracellular lipid bodies was expected to be 1-2 orders of magnitude higher than signals resulting from ion concentration gradients in the absence of absorption-based resonance effects.

THG imaging of lipid bodies in liver cells and tissue

We recorded THG images of hepatocytes (**Fig. 1a**) and fresh rat liver tissue (**Fig. 1b**) upon 1,180 nm excitation. We confirmed the third-harmonic nature of the signal by verifying its third-order dependence on excitation intensity and its forward-directed emission in isolated cells.

Micrometer-sized intracellular structures appeared as readily detectable bright spots in the THG images, with a peak signal of ~20–30 detected photons/μs under 90 mW, 0.8 NA illumination. These structures were detected with high specificity because they produce a third-harmonic signal 20–100 times higher than other cellular components (**Fig. 1a**). To check whether lipid bodies are responsible for this signal, we stained fixed isolated hepatocytes with Nile Red, a hydrophobic fluorescent dye that accumulates in lipid bodies[6]. We recorded simultaneously 2PEF images of Nile Red distribution and THG images. As evident from the three-dimensional (3D) reconstructions in **Figure 1c** and **Supplementary Video 1** online, the two images are perfectly correlated, confirming that lipid bodies are responsible for the highly contrasted features in the THG image. These data also illustrate that the 3D resolution of THG microscopy is comparable to that of 2PEF microscopy. We compared cell viability in illuminated and control cells and found that cell survival rate, enzymatic activity and division were unaffected by THG observation, indicating that volume scanning did not induce substantial damage to the hepatocytes (see methods and **Supplementary Data** online).

We directly used this endogenous signal to quantify the size distribution of lipid bodies under different physiological conditions, by recording image stacks of hepatocytes isolated from tissue under normal conditions and from a regenerating liver 24 h after a partial hepatectomy (**Fig. 1d** and **Supplementary Figure 1** online). As reported earlier, rodent liver transiently becomes fat after partial hepatectomy[16], but the mechanisms and physiological relevance of this are still not completely understood[17]. The histograms in **Figure 1d** reflect this altered metabolism, and show that THG microscopy directly provides a quantitative description of the physiological state of the regenerating hepatocytes. Finally, we point out that the same information can be extracted from images of unstained fresh tissue (**Fig. 1b**).

Tracking lipid bodies in developing embryos

It is generally difficult to study the trafficking dynamics of lipid bodies *in vivo* because of a lack of appropriate techniques. A system

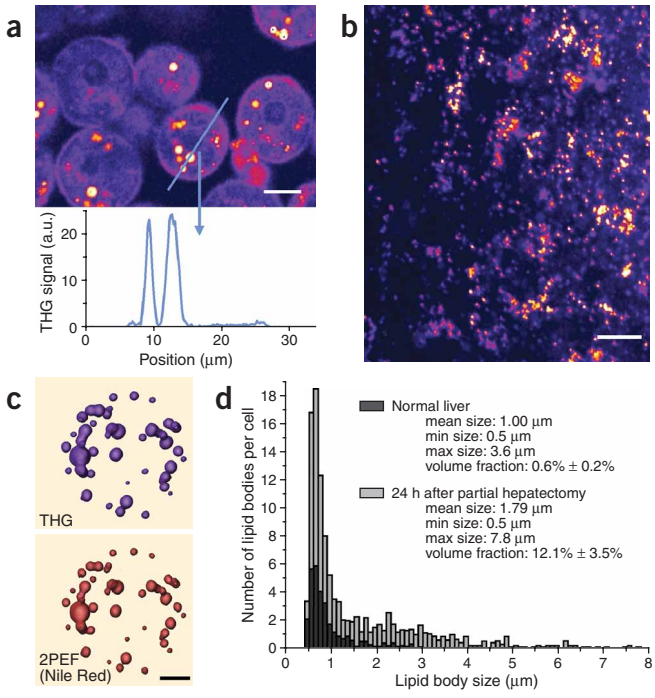

Figure 1 | Lipid bodies are the main source of contrast in THG images of hepatocytes and liver tissue. (**a**) THG image of freshly isolated hepatocytes (top). Acquisition time, 1.2 s. Bar, 10 μm. Profile along the blue line in the top panel (bottom). (**b**) THG image of perfused liver tissue (projection of 30 images recorded 2 μm apart). Total imaging time 2 min. Bar, 20 μm. (**c**) Hepatocytes stained with Nile Red imaged simultaneously with THG (top) and 2PEF (bottom). 3D reconstruction calculated from 100 images recorded 0.2 μm apart. Acquisition time, 0.6 s per two-dimensional image and 25 s for a complete 3D image. Bar, 5 μm. (**d**) Size distribution of lipid bodies in normal cells ($n = 17$) and regenerating cells ($n = 10$), as measured from 3D THG images. See also **Supplementary Figure 1**.

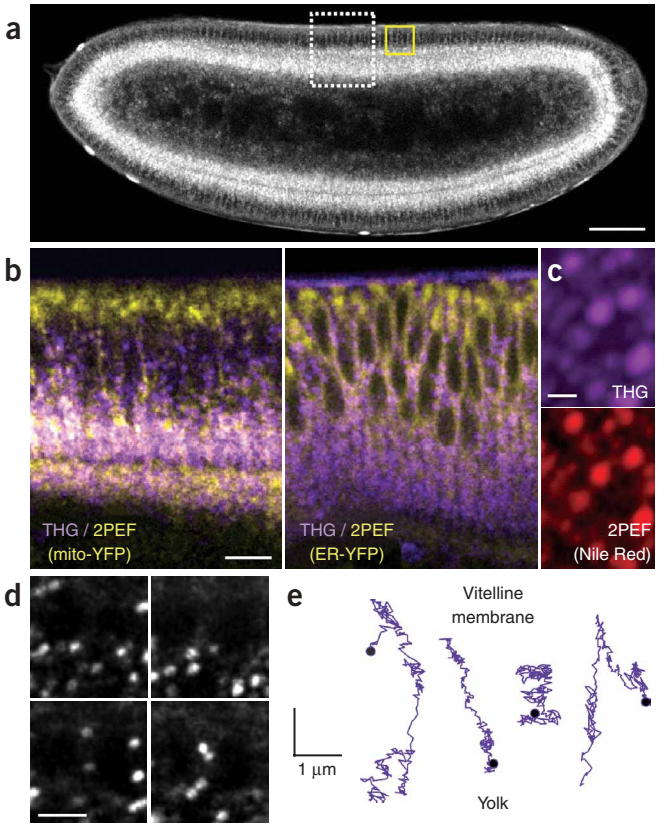

Figure 2 | Lipid bodies trafficking dynamics can be studied in gastrulating *D. melanogaster* embryos using THG microscopy. (**a**) THG image of a *D. melanogaster* embryo before gastrulation. Acquisition time, 2.5 s. Bar, 50 μm. (**b**) Simultaneous THG (purple) and 2PEF (yellow) images of YFP-tagged embryos, revealing the distinct localization of THG signal, mitochondria (left) and endoplasmic reticulum (right). The imaged regions correspond to the dashed white box in **a**. Imaging time, 1 s. Bar, 5 μm. (**c**) Nile Red staining of fixed embryos (bottom) confirms that the THG signal (top) arises from lipid bodies. Bar, 2 μm. Imaging time, 5 s. (**d**) Images extracted from a 5-min sequence showing the trafficking dynamics of lipid bodies *in vivo*. The imaged region corresponds to the yellow box in **a**. Acquisition time, 290 ms per image. Bar, 5 μm. See **Supplementary Video 2**. (**e**) Typical trajectories of trafficking lipid bodies over 30 s. Temporal resolution, 120 ms. See **Supplementary Video 3**.

of particular interest is the rapid bidirectional transport of vesicles in *D. melanogaster* embryos before gastrulation. During the process of cellularization, lipid droplets undergo dynein-driven transport, and there are characteristic changes in their distribution that have been studied in artificially compressed embryos with transmitted-light microscopy[18]. Recent studies have reported that large-scale THG imaging can provide structural images of unstained embryos[11,19,20]. In particular, we observed a strong THG signal around the central yolk region and around cell nuclei in early *D. melanogaster* embryos (**Fig. 2a**). When imaging the entire embryo, this signal delineates the cells and can be used to characterize morphogenetic movements[19,21]. At a microscopic scale, the signal is found to originate principally from very mobile micrometer-scale structures. To verify the origin of the THG signal, we recorded combined 2PEF-THG image sequences of YFP-tagged transgenic embryos during cellularization and gastrulation. We used three transgenic lines in which YFP was localized in the mitochondria, the endoplasmic reticulum (**Fig. 2b**) or the Golgi apparatus (data not shown). In either case, the localization and distribution dynamics of the labeled component, as visualized by 2PEF, were clearly distinct from the structures visible in the THG images. Alternatively, we stained fixed gastrulating embryos with Nile Red and recorded combined 2PEF-THG images (**Fig. 2c**), which exhibited excellent correlation. Together, these data confirm that lipid bodies are detected by THG microscopy in live embryos. The strong signal obtained from individual droplets allows fast imaging and individual lipid body tracking *in vivo* (**Fig. 2d**,**e**, and **Supplementary Videos 2** and **3** online). For example, we recorded the trajectories displayed in **Figure 2e** with 120 ms time resolution. A benefit of THG imaging over conventional techniques is that it provides 3D resolution and deeper penetration in scattering samples. It can therefore be used in uncompressed embryos, which preserves their viability[19]. More generally, it should be possible to track the fate of mobile lipid bodies in numerous systems and tissues.

THG imaging of lipid bodies in plant seeds

As lipid storage and mobilization are central in plant development[1], we also assessed the potential of THG microscopy to characterize lipid accumulation in plant tissue. We focused on nongreen tissue and recorded images of seeds from various species with different lipid concentrations: *Arabidopsis thaliana*, *Medicago truncatula*, *Brassica napus* (oilseed rape) and *Glycine max* (soybean). **Figure 3a** is a THG image of an intact *A. thaliana* seed harvested from its silique, where bright particle-like structures are detected in cell layers constituting the embryo sack. Nile Red labeling confirmed that these particles are lipid-rich bodies (**Fig. 3b**).

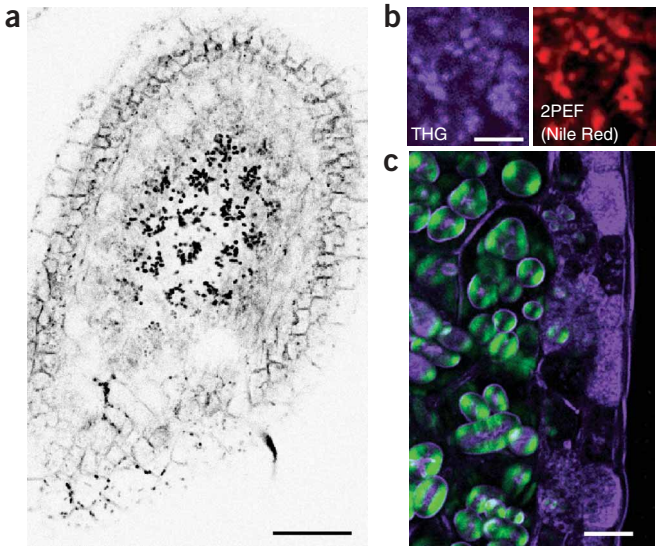

Figure 3 | THG imaging of plant seed tissue. (**a**) THG image of an intact unstained *A. thaliana* seed harvested from its silique, recorded 50 μm below the seed surface. Bar, 50 μm. (**b**) Simultaneous THG (left) and 2PEF (right) images from a similar region of a Nile Red–labeled *A. thaliana* seed section. Bar, 10 μm. (**c**) Simultaneous THG (purple) and SHG (green) images recorded from an unstained soybean seed section. SHG is due to starch granules, whereas the THG image reveals the presence of a lipid-rich cell layer at the seed peripheral region (right side of the image). Bar, 25 μm.

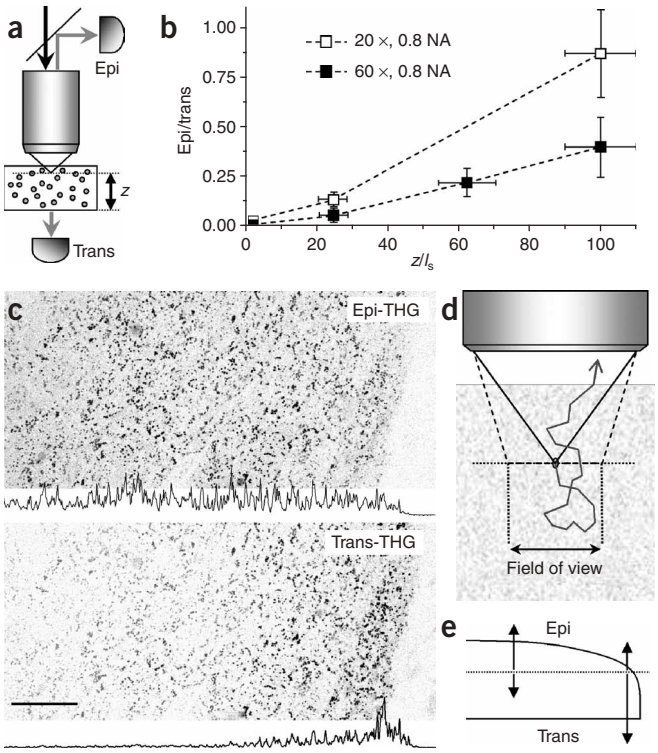

Figure 4 | Epi-detected imaging is possible in weakly absorbing tissues owing to THG light backscattering. (**a**) Experimental geometry for characterizing the influence of third-harmonic light scattering on the epi/trans signal ratio in THG imaging. The sample consists of microspheres (Sigma) embedded in an agarose gel of adjustable scattering properties. z denotes the gel thickness below the focal plane. Black arrow, excitation light ($\lambda = 1{,}180$ nm). Gray arrows, THG light. (**b**) Ratio of the epi-THG signal to the trans-THG signal plotted as a function of the number of scattering mean free paths (z/l_s^{THG}) under the focal point. Epicollection is more efficient for a highly scattering medium and a low-magnification objective. (**c**) Epi- (top) and trans- (bottom) THG images of a thick mouse lung sample (tissue geometry described in **e**. The signal intensity profile as a function of the position is shown under each image. Imaging time, 10 s. Scale bar, 50 μm. (**d**) An extended field of view provides a more efficient collection of backscattered light. (**e**) Geometry of the tissue where images in **c** were recorded.

Similar observations were performed in seed tissue from other species. In particular, we found that THG imaging can detect the presence of large (5–20 μm) lipid inclusions in *B. napus* seed tissue (particularly rich in lipids), which are not present in *M. truncatula* or soybean samples (**Supplementary Figure 2** online). We note that plant cell walls also give a detectable signal, which is possibly related to their structure. Finally, the same laser beam can be used to simultaneously detect starch granules by taking advantage of their SHG properties[22]. **Figure 3c** is a combined SHG-THG image of unstained soybean seed tissue, in which lipid-rich cell layers are detected in peripheral seed regions, next to starch storage areas.

Epi-THG imaging is possible in weakly absorbing tissues

Having shown that micrometer-sized lipid bodies can be selectively detected in various environments, it is of practical relevance to consider the possibility of epi-detected THG imaging of tissues. For finite-sized heterogeneities and interfaces at the beam focus, the THG radiation is expected to be highly directional and emitted in the direction of the excitation beam[9,12]. Therefore THG microscopy is in principle a transmitted-mode technique, which restricts its application to thin samples (typically 2–3 mm or less). When imaging inside a biological tissue, however, bulk scattering can redirect an appreciable fraction of the forward-emitted third-harmonic radiation back to the tissue surface, provided that THG light is not reabsorbed by the tissue. When it reaches the surface, backscattered light seems to originate from an extended source within the tissue and is more efficiently collected with a low-magnification objective that provides an extended lateral field of view (**Fig. 4**), as demonstrated for deep-tissue 2PEF microscopy[23,24]. To experimentally address this issue, we analyzed trans- and epi-detected THG images of polystyrene beads near the surface of nonabsorbing agarose gels with known scattering characteristics (**Fig. 4a**). Epi-detected images were recorded using two objectives with similar NA ($\sim$0.8) but different magnifications (60× and 20×). The epi/trans ratio is presented in **Figure 4b** as a function of the thickness of the gel in units of scattering mean free paths. These data confirm that although micrometer-sized inclusions principally produce third-harmonic light in the forward direction (see vanishing epi/trans ratio in a transparent gel, $z/l_s \approx 0$ in **Fig. 4b**), bulk scattering can redirect an important fraction of this light toward the objective. Moreover, the use of a low-magnification, high-NA objective makes it possible to efficiently collect this backscattered component while preserving the resolution. We confirmed that these observations apply to tissue imaging by recording epi- and trans-THG images of a $\sim$800-μm-thick slice of fresh lung tissue in the geometry depicted in **Figure 4e**. Epi-detected imaging is possible where the tissue is thick, and detection is less efficient near the tissue border where scattered light may definitively exit the tissue without reaching back to the objective (**Fig. 4c**). In contrast, the transmission signal is higher near the tissue border because of reduced scattering of the excitation beam.

Multimodal histology of unstained lung tissue

THG microscopy is a relatively simple nonlinear imaging technique because it requires a single excitation beam. Appropriate wavelengths are commonly obtained from an optical parametric oscillator (OPO) driven by a femtosecond titanium:sapphire (Ti:S) source; in this configuration, it is straightforward to combine THG imaging with SHG and 2PEF imaging and to take advantage of the tunability of the Ti:S source. This approach allows one to map several tissue components exhibiting characteristic nonlinear responses[8], along with lipid bodies. For example, **Figure 5** contains multimodal images of fresh rat lung tissue. In the THG images (for example, **Fig. 5a**), the primary source of contrast is composed of micrometer-sized structures that have a particularly dense distribution near the pleura. Nile Red accumulates in these structures (**Fig. 5b**), which suggests that the signal likely originates from surfactant lamellar bodies[25] and/or vitamin A storage vesicles[26]. This latter hypothesis is supported by the fact that most of the detected structures exhibit fluorescence with spectral characteristics of retinol (**Supplementary Figure 3** online). Along with the distribution of lipid bodies revealed by the THG data, SHG images map the distribution of collagen fibers[8] near the pleura; the 2PEF signal recorded with 860-nm excitation is principally due to elastin fibers[8] and reveals the alveolar morphology; a component of the

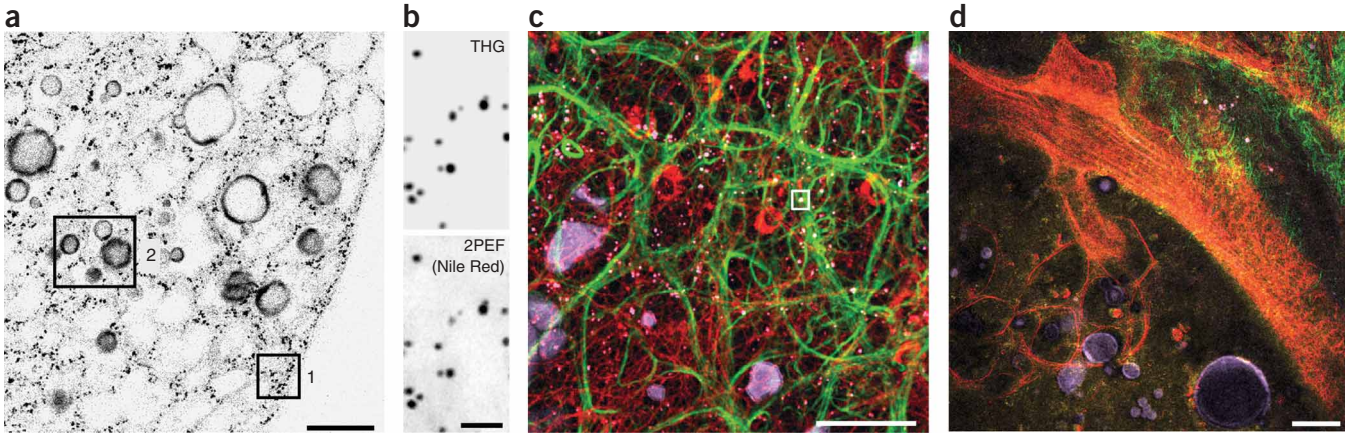

Figure 5 | Multimodal multiphoton imaging of fresh lung tissue. (**a**) Typical THG image recorded 40 μm below the surface of a thick slice of mouse lung tissue, in which the contrast has been enhanced to outline the various structures seen in the image. The signal mainly arises from lipid bodies (square 1) and air bubbles contained in alveolar sacs (square 2; air bubbles produce a peak signal ~3× less than that of lipid bodies). Bar, 50 μm. (**b**) Simultaneous 2PEF-THG images of Nile Red–stained tissue. Imaging time, 0.9 s. Bar, 5 μm. (**c**,**d**) Unstained rat lung tissue observed using THG-SHG-2PEF microscopy. THG imaging (1,180 nm excitation, purple and white) reveals the distribution of micrometer-sized lipid bodies and large air bubbles; SHG imaging (860 nm excitation, green) maps fibrillar collagen; 2PEF imaging detects elastin fibers, flavoproteins, retinol (860 nm excitation, red) and NADH (700 nm excitation, yellow; **d** only). The emission spectrum of a region containing fluorescent lipid bodies and collagen fibrils (white square in **c**) was measured, and the results are shown in **Supplementary Figure 3**. Bars, 50 μm.

signal is also attributable to cellular fluorophores such as retinol and possibly flavoproteins[27]. Finally, the 2PEF signal recorded with 700-nm excitation originates mainly from NADH and reflects the local redox state[27,28]. Given the efficiency of the various nonlinear processes involved, such images can be recorded within rapid acquisition times without apparent alteration of the tissue. Using our setting, a few seconds of exposure were necessary for each excitation wavelength, resulting in typically 3-min acquisition time for a full four-color image. This time could be reduced to 10–30 s with an automated tunable laser. The ability to detect lipid bodies including retinoid stores, along with extracellular matrix components and redox state in intact lung tissue may provide a unique tool to study processes such as organogenesis and alveolus formation[26].

DISCUSSION

Our data establish that lipid bodies can be specifically detected in unstained cells and tissues using THG microscopy with 1,100–1,200-nm excitation. The advantage of this approach is that it provides 3D spatial resolution and can be used to study lipid bodies in a complex environment. Moreover, long-term observation is possible because harmonic generation does not involve energy deposition in the sample, and therefore does not suffer from photobleaching. Few other methodologies can provide a direct visualization of unstained lipid bodies *in situ*. Coherent anti-Stokes Raman scattering microscopy has been proposed as a promising possibility[29] with the benefit of providing vibrational spectra; but it requires more complex laser systems. An attractive aspect of THG microscopy is that it can be easily implemented on a conventional 2PEF-SHG microscope by extending the excitation wavelength range.

THG being a weak process, rapid imaging requires instantaneous intensities in the TW/cm^2 regime. Such conditions typically induce photodestructive effects when using wavelengths in the 700–900 nm range[21]. Therefore, one key point in achieving sustained THG imaging is to use excitation wavelengths for which one-photon and two-photon absorption are minimal. Under such conditions, we found that repeated imaging preserves cell viability and division. We also note that when exciting unstained tissues with pulsed 1,100–1,200-nm light, THG from lipid bodies is generally more efficient than three photon–excited fluorescence from endogenous fluorophores, likely because of coherence enhancement[14].

The demonstrated possibility of efficient epidetection brings convenience for the observation of thick samples. Epidetection, however, requires that the absorption mean free path of third-harmonic light in the tissue is longer than its reduced scattering mean free path[30]. For example, in highly vascularized tissues, blood cells could reabsorb the ~400-nm radiation before it escapes the tissue. This issue might be examined by using an appropriate excitation wavelength, or by perfusing the tissue with a saline solution. We also note that deep THG imaging is very sensitive to excitation scattering because the signal scales with the cube of excitation intensity. In lung tissue, we found that the signal approximately scaled as $\exp(-z/40\ \mu m)$, and that the imaging depth was principally limited by the available OPO power, typically to 80 μm. This depth could be increased by redistributing the power into higher energy pulses, as demonstrated for deep-tissue 2PEF[31,32] or by incorporating a wavefront-correction scheme into the microscope.

Until now, it has been difficult to perform real-time studies of lipid bodies *in situ*. The methodology reported here opens many possibilities for studying physiological activity of intact cells and tissues. THG microscopy should allow monitoring the transport, size and aggregation of lipid bodies, depending on their composition and structure and on cell physiological conditions. More generally, its combination with techniques like SHG or 2PEF imaging provides a new tool for studying regulation of lipid bodies along with the distribution of extracellular matrix components and cellular redox state in intact tissue, and may prove useful in understanding physiological processes involved in organ development, inflammatory response and deregulated fat metabolism

observed in common diseases such as atherosclerosis, diabetes and liver steatosis[33].

METHODS

Nonlinear microscopy. We performed the imaging experiments on a custom-built multiphoton microscope incorporating a femtosecond Ti:S oscillator (Coherent, Inc.), an optical parametric oscillator (OPO; APE), galvanometer mirrors (GSI Lumonics), water-immersion objectives (0.8–0.9 NA; Olympus) and photon-counting photomultiplier (PMT) modules (Electron Tubes). We implemented simultaneous detection channels in the forward and backward directions. We recorded the THG images using 90 mW, 1,180 nm excitation, 10–40 μm/ms scanning speed, and an interference filter (390 nm) in the detection channel. We detected THG in the transmitted direction, except for lung tissue experiments, in which we used both epi and trans signals. Depending on the application, we performed 2PEF and SHG imaging using 700 nm, 860 nm or 1,180 nm excitation wavelengths. Objectives are not chromatically corrected for this range, resulting in different imaging planes. We reduced this offset to 3 μm by adjusting the divergence of the OPO beam, and corrected the remaining difference by moving the objective when switching wavelengths. Image analysis was performed using ImageJ (W. Rasband, National Institute of Health, Maryland, USA) and AMIRA (Mercury Computer Systems). We note that a standard multiphoton (2PEF) microscope can be adapted for THG imaging as described here by extending the excitation wavelength range to the 1,050–1,250 nm region. This can be done by associating an OPO to the Ti:S source, or by using a longer-wavelength laser (for example, Cr:Forsterite).

Measurements of liquid nonlinear susceptibility and dispersion. We measured nonlinear susceptibilities as described[15]. We introduced the liquid sample in a wedge-shaped cell of thickness ranging from 0 to 100 μm. We used two cells made respectively from fused silica and from BK7 glass to characterize the solutions using published reference values[34]. The excitation beam was weakly focused (NA $\approx$ 0.1) at the middle of the cell, and the THG signal was measured in the transmitted direction. We recorded maker fringes when increasing the thickness of the cell. The amplitude of the fringes is proportional to $| \chi_g^{(3)}/n_{g,3\omega}(n_{g,3\omega} - n_{g,\omega}) - (t_{lg}{}^{3\omega}/(t_{lg}{}^{\omega})^3)\ \chi_l^{(3)}/n_{l,3\omega}(n_{l,3\omega} - n_{l,\omega})\ |^2$, where the indices g and l refer to glass and liquid, respectively, $\chi^{(3)}$ is the third-order nonlinear susceptibility, $n_{3\omega}$ is the refractive index at the harmonic frequency, $(n_{3\omega} - n_{\omega})$ is the refractive index dispersion between harmonic and fundamental frequencies and $t_{ij}^{n\omega}$ are transmission coefficients at the interfaces. The above equation assumes that $t_{lg}{}^{3\omega}\ t_{gl}{}^{3\omega} \approx (t_{lg}{}^{\omega}\ t_{gl}{}^{\omega})^3$, which was verified in our conditions. When not available in the literature, we deduced $(n_{l,3\omega} - n_{l,\omega})$ from the fringe period. We used water as a reference to normalize the signal amplitude and calculated the nonlinear susceptibilities by combining the results obtained with the BK7 and fused silica cells. Measurements of $(n_{l,3\omega} - n_{l,\omega})$ were the main source of uncertainty.

Viability assays. Cell viability after 3D imaging was verified by comparing trypan blue exclusion and calcein acetoxymethyl ester (calcein-AM) hydrolysis in illuminated and unilluminated cells (**Supplementary Data**).

Additional methods. All sample preparation and labeling methods are described in the **Supplementary Methods** online.

Note: Supplementary information is available on the Nature Methods website.

ACKNOWLEDGMENTS

We thank M. Welte (Brandeis University, Waltham, Massachusetts, USA) for advice on embryo staining, G. Ephritikhine (Institut des Sciences du Végétal, Gif-sur-Yvette, France) for help with the plant experiments, J.-M. Sintes and X. Solinas for assistance in microscope design, S. Boucherie for assistance in hepatocytes preparation, and J.-L. Martin and J. Ogilvie for critical comments. This work was supported by the Délégation Générale pour l'Armement.

COMPETING INTERESTS STATEMENT

The authors declare that they have no competing financial interests.

Published online at http://www.nature.com/naturemethods/
Reprints and permissions information is available online at http://npg.nature.com/reprintsandpermissions/

1. Murphy, D.J. The biogenesis and functions of lipid bodies in animals, plants and microorganisms. *Prog. Lipid Res.* **40**, 325–438 (2001).
2. Martin, S. & Parton, R.G. Caveolin, cholesterol, and lipid bodies. *Semin. Cell Dev. Biol.* **16**, 163–174 (2005).
3. Murphy, D.J. & Vance, J. Mechanisms of lipid-body formation. *Trends Biochem. Sci.* **24**, 109–115 (1999).
4. Imanishi, Y., Gerke, V. & Palczewski, K. Retinosomes: new insights into intracellular managing of hydrophobic substances in lipid bodies. *J. Cell Biol.* **166**, 447–453 (2004).
5. Heid, H.W. & Keenan, T.W. Intracellular origin and secretion of milk fat globules. *Eur. J. Cell Biol.* **84**, 245–258 (2005).
6. Greenspan, P., Mayer, E.P. & Fowler, S.D. Nile red: a selective fluorescent stain for intracellular lipid droplets. *J. Cell Biol.* **100**, 965–973 (1985).
7. Zipfel, W.R., Williams, R.M. & Webb, W.W. Nonlinear magic: multiphoton microscopy in the biosciences. *Nat. Biotechnol.* **21**, 1369–1377 (2003).
8. Zipfel, W.R. *et al.* Live tissue intrinsic emission microscopy using multiphoton-excited native fluorescence and second-harmonic generation. *Proc. Natl. Acad. Sci. USA* **100**, 7075–7080 (2003).
9. Barad, Y., Eisenberg, H., Horowitz, M. & Silberberg, Y. Nonlinear scanning laser microscopy by third harmonic generation. *Appl. Phys. Lett.* **70**, 922–924 (1997).
10. Squier, J.A., Müller, M., Brakenhoff, G.J. & Wilson, K.R. Third harmonic generation microscopy. *Opt. Express* **3**, 315–324 (1998).
11. Oron, D. *et al.* Depth-resolved structural imaging by third-harmonic generation microscopy. *J. Struct. Biol.* **147**, 3–11 (2004).
12. Boyd, R.W. *Nonlinear optics* 2nd edn. (Academic Press, San Diego, 2003).
13. Cheng, J.-X. & Xie, X.S. Green's function formulation for third harmonic generation microscopy. *J. Opt. Soc. Am. B* **19**, 1604–1610 (2002).
14. Débarre, D., Supatto, W. & Beaurepaire, E. Structure sensitivity in third-harmonic generation microscopy. *Opt. Lett.* **30**, 2134–2136 (2005).
15. Kajzar, F. & Messier, J. Original technique for third-harmonic-generation measurements in liquids. *Rev. Sci. Instr.* **58**, 2081–2085 (1987).
16. Delahunty, T.J. & Rubinstein, D. Accumulation and release of triglycerides by rat liver following partial hepatectomy. *J. Lipid Res.* **11**, 536–543 (1970).
17. Shteyer, E., Liao, Y., Muglia, L.J., Hruz, P.W. & Rudnick, D.A. Disruption of hepatic adipogenesis is associated with impaired liver regeneration in mice. *Hepatology* **40**, 1322–1332 (2004).
18. Welte, M.A., Gross, S.P., Postner, M., Block, S.M. & Wieschaus, E.F. Developmental regulation of vesicle transport in *Drosophila* embryos: forces and kinetics. *Cell* **92**, 547–557 (1998).
19. Débarre, D. *et al.* Velocimetric third-harmonic generation microscopy: micrometer-scale quantification of morphogenetic movements in unstained embryos. *Opt. Lett.* **29**, 2881–2883 (2004).
20. Sun, C.-K. *et al.* Higher harmonic generation microscopy for developmental biology. *J. Struct. Biol.* **147**, 19–30 (2004).
21. Supatto, W. *et al. In vivo* modulation of morphogenetic movements in *Drosophila* embryos with femtosecond laser pulses. *Proc. Natl. Acad. Sci. USA* **102**, 1047–1052 (2005).
22. Cox, G., Moreno, N. & Feijo, J. Second-harmonic imaging of plant polysaccharides. *J. Biomed. Opt.* **10**, 024013 (2005).
23. Beaurepaire, E. & Mertz, J. Epifluorescence collection in two-photon microscopy. *Appl. Opt.* **41**, 5376–5382 (2002).
24. Oheim, M., Beaurepaire, E., Chaigneau, E., Mertz, J. & Charpak, S. Two-photon microscopy in brain tissue: parameters influencing the imaging depth. *J. Neurosci. Methods* **111**, 29–37 (2001).

25. Dietl, P. & Haller, T. Exocytosis of lung surfactant: from the secretory vesicle to the air-liquid interface. *Annu. Rev. Physiol.* **67**, 595–621 (2005).
26. Dirami, G. *et al.* Lung retinol storing cells synthesize and secrete retinoic acid, an inducer of alveolus formation. *Am. J. Physiol. Lung Cell. Mol. Physiol.* **286**, L249–L256 (2004).
27. Huang, S., Heikal, A.A. & Webb, W.W. Two-photon fluorescence spectroscopy and microscopy of NAD(P)H and flavoprotein. *Biophys. J.* **82**, 2811–2825 (2002).
28. Patterson, G.H., Knobel, S.M., Arkhammar, P., Thastrup, O. & Piston, D.W. Separation of the glucose-stimulated cytoplasmic and mitochondrial NAD(P)H reponses in pancreatic islet beta cells. *Proc. Natl. Acad. Sci. USA* **97**, 5203–5207 (2000).
29. Nan, X., Cheng, J.-X. & Xie, X.S. Vibrational imaging of lipid droplets in live fibroblast cells with coherent anti-Stokes Raman scattering microscopy. *J. Lipid Res.* **44**, 2202–2208 (2003).
30. Niemz, M.H. *Laser-Tissue Interactions: fundamentals and Applications* (Springer, Berlin, 2004).
31. Theer, P., Hasan, M.T. & Denk, W. Two-photon imaging to a depth of 1000 μm in living brains by use of a TiAl2O3 regenerative amplifier. *Opt. Lett.* **28**, 1022–1024 (2003).
32. Beaurepaire, E., Oheim, M. & Mertz, J. Ultra-deep two-photon excitation in turbid media. *Opt. Commun.* **188**, 25–29 (2001).
33. Day, C.P. & James, O.F.W. Hepatic steatosis: Innocent bystander or guilty party? *Hepatology* **27**, 1463–1466 (1998).
34. Bosshard, C., Gubler, U., Kaatz, P., Mazerant, W. & Meir, U. Non-phase-matched optical third-harmonic generation in noncentrosymmetric media: cascaded second-order contributions for the calibration of third-order nonlinearities. *Phys. Rev. B* **61**, 10688–10701 (2000).
35. Wohlfarth, C. & Wohlfarth, B. *Landolt-Börnstein Numerical data and functional relationships in science and technology* (New Series III/38A et B) (Springer-Verlag, Berlin, 1996).
36. Nikogosyan, N.D. *Properties of Optical and Laser-related materials: a handbook* (Wiley, Chichester, 1997).